An Experimental Study of the Unsteady Aerodynamics of a Static DU91-W2-150 Airfoil at Large Angles of Attack

Xu, Guanqun; Yu, Wei; Sciacchitano, Andrea; Simao Ferreira, Carlos

DOI
10.1002/we.2974

Publication date
2025

Document Version
Final published version

Published in
Wind Energy

Citation (APA)
Xu, G., Yu, W., Sciacchitano, A., & Simao Ferreira, C. (2025). An Experimental Study of the Unsteady Aerodynamics of a Static DU91-W2-150 Airfoil at Large Angles of Attack. *Wind Energy*, *28*(3), Article e2974. https://doi.org/10.1002/we.2974

Wind Energy

WILEY

RESEARCH ARTICLE OPEN ACCESS

An Experimental Study of the Unsteady Aerodynamics of a Static DU91-W2-150 Airfoil at Large Angles of Attack

Guanqun Xu | Wei Yu | Andrea Sciacchitano | Carlos Simao Ferreira

Faculty of Aerospace Engineering, Delft University of Technology, Deft, Netherlands

Correspondence Wei Yu (W.Yu@tudelft.nl)

Received: 10 February 2024 | **Revised:** 30 October 2024 | **Accepted:** 27 December 2024

Funding: No funding is used for the research.

Keywords: airfoil Strouhal number | large angle of attack | particle image velocimetry (PIV) | pressure measurement | unsteady aerodynamics | vortex shedding

ABSTRACT

The airfoil DU91-W2-150 was investigated in the Low Speed Low Turbulence Tunnel at the Delft University of Technology to study unsteady aerodynamics. This experimental study tested the airfoil under a wide range of angles of attack (AoA) from 0° to 310° at three Reynolds numbers (*Re*) from 2×10^5 to 8×10^5. Pressure on the airfoil surface was measured and particle image velocimetry (PIV) measurements were conducted to capture the flow field in the wake. By examining the force coefficient and comparing the wake contours, it shows that an upwind concave surface provides a higher load compared to a convex surface upwind case, highlighting the critical role of surface shape in aerodynamics. When comparing separation at specific locations along the chord for all three *Re* values, it is observed that as *Re* increases, separation tends to occur at lower AoA, both for positive stall and negative stall. The examination of the aerodynamic force variation indicates that, during reverse flow, fluctuations are more pronounced compared to forward flow. This is owing to separation occurring at the aerodynamic leading edge (geometric trailing edge) in reverse flow. In terms of vortex shedding frequency, the study found a nearly constant normalized Strouhal number (*St*) of 0.16 across various *Re* and AoA values in fully separated regions, indicating a consistent pattern under these conditions. However, a slight increase in *St*, between 0.16 and 0.20, was observed for AoA values exceeding 180°, possibly due to the convex curvature of the airfoil in the upwind direction. In conclusion, this research not only corroborates previous findings for small AoA values but also adds new data on the aerodynamic behavior of the DU91-W2-150 airfoil under large AoA values, offering various perspectives on the effects of surface curvature, *Re*, and flow conditions on key aerodynamic parameters.

1 | Introduction

The field of wind turbine aerodynamics, which deals with the interaction between wind and wind turbine blades and tower, is constantly attracting much focus. Notably, the aerodynamics governing the behavior of an airfoil on a wind turbine blade assumes critical significance, given its direct influence on the airfoil's force dynamics and, consequently, the overall power generation. Nevertheless, the complexities inherent to the unsteady aerodynamics of airfoils, attributed to the flow characteristics and airfoil geometry, pose significant challenges when it comes to experimental investigations or numerical simulations [1].

As an airfoil pitches up to a certain angle of attack (AoA), separation can occur at the suction side of the airfoil surface. This is due to the increase in the adverse pressure gradient; the larger the adverse pressure gradient, the earlier the flow separation occurs. The separation can be characterized as open or closed. Closed separations are usually referred to as separation bubbles [2], where the flow first detaches from and then reattaches onto the surface of an airfoil. A laminar separation bubble (LSB) can be identified by the plateauing of the surface pressure, starting from the separation point and ending before the transition to turbulence flow [3]. Conversely, open separation occurs when the separated boundary layer interacts and mixes with free shear layers, usually shown as "dead air" in the wake of an airfoil, with the pressure equivalent to that of a free stream [2].

Surface pressure measurements in wind tunnels are often employed to characterize the instantaneous pressure distributions over airfoils. Stall behavior was investigated with pressure taps in the tunnel with a maximum AoA of 20° [4]. Interestingly, by comparing three layouts of pressure tapping, locations of separation and reattachment were compared [5]. In another research [6], the unsteady loads of a NACA0021 airfoil at large AoA values up to 90° were studied, investigating the *St* number beyond the stall angle. The effect of the LSB with the AoA up to 20° was discussed [3]. The vortex shedding of the airfoil NACA0018 at AoA of 10° was experimentally studied, and it was found that the vortex shedding frequency scales with the cross-flow distance between the two wake vortices under different *Re* [7]. Both pressure tap measurements and microphone measurements were conducted for the NACA0018 airfoil and the flow regions at AoA values of 8° and 12° were compared [8]. The above-mentioned studies are listed below in Table 1. These research findings contribute essential knowledge into airfoil aerodynamics at low AoA; however, further investigation is needed to fully understand the behavior of airfoils at high AoA.

Recent studies have increasingly focused on airfoil behavior at large AoA. Timmer [9] compared several wind tunnel campaigns across various airfoil profiles, highlighting general trends in maximum drag coefficient and lift-drag ratio, though the underlying flow physics remains largely unexplored. Lind and Jones [10] experimentally investigated vortex shedding from static airfoils over a full range of AoA, with particular emphasis on the reverse flow region (150° to 180°). They identified three distinct reverse flow regions by comparing sharp and blunt trailing edge airfoils. In a follow-up study, Lind and Jones further analyzed pressure distributions on the airfoil surface at large AoA values between 0° and 180° [11], providing key insights into the mechanisms and frequencies of vortex shedding for symmetric airfoils. However, given the prevalence of asymmetric airfoil profiles in wind turbine applications, further research is needed to explore vortex shedding behavior in these more complex geometries.

In several situations, wind turbine blades experience very high AoA: those include when a wind turbine experiences an extreme change in the wind direction, during yaw misalignment, and in parked conditions. At high AoA values, the blade sections behave like a bluff body rather than a streamlined airfoil [12]. In this scenario, vortices are shed periodically from the blades, and vortex-induced vibrations (VIV) can occur for slender blades. Detailed discussion on VIV can be found in review papers [13, 14]. While some simulation studies have investigated VIV in wind turbine blades [15, 16], the detailed flow physics at the airfoil level—particularly related to high AoA values—remains unknown, leaving the fundamental mechanisms behind VIV unresolved.

To investigate the aerodynamic perspective of VIV on wind turbine blades at the airfoil level, this research aims to experimentally study the unsteady aerodynamic characteristics of the static airfoil DU91-W2-150 in a wide range of AoA values from 0° to 310°, with a focus on the wake flow dynamics, vortex shedding characteristics, and airfoil loading. The experiments were performed at *Re* numbers of 2×10^5, 5×10^5, and 8×10^5. Pressure taps were mounted over the airfoil surface to measure the static pressure and in turn the aerodynamic loads and forces.

Particle image velocimetry (PIV) is a measurement technique that allows the quantitative visualization of fluid flows. In the last years, PIV has been widely used for studying the flow around airfoil sections [17–19]. In this campaign, planar PIV measurements were conducted to visualize the wake flow field under different *Re* and AoA values. Meanwhile, proper orthogonal decomposition (POD) analysis is applied to PIV images to extract the most important flow structures in the airfoil wake region.

2 | Methodology

2.1 | Experimental Setup and Test Cases

The experiment was conducted in the Low Speed Low Turbulence Tunnel at the Delft University of Technology. The wind tunnel has a maximum wind speed of 120 m/s and *Re* up to 3.5×10^6 for two-dimensional testing. It has a large contraction ratio of 18.7, which yields a maximum turbulence intensity

TABLE 1 | Unsteady aerofoil experimental research.

Reference	Airfoil	Method	AoA (°)	$Re\,(-)$
[4]	NACA0015, NACA63-418 RISØ-B1-18, RISØ-C2-1	Pressure taps	6–20	1.6×10^6 to 6×10^6
[5]	S8036	Pressure taps, surface flow visualisation	4–14	7.5×10^3 to 2×10^5
[6]	NACA0021	Pressure taps	0–90	2.7×10^5
[3]	NACA0012 and NACA4412	Pressure taps	−6–20	5×10^4 to 2×10^5
[7]	NACA0018	Pressure taps	10	3×10^4 to 2×10^5
[8]	NACA0018	Pressure taps and microphones	8 and 12	1×10^5

of 0.2% at maximum speed [20]. The test section has a size of 1.80 m high, 1.25 m wide, and 2.60 m long. The inner side view of the test section is shown on the left in Figure 1.

The asymmetric profile DU91-W2-150 was used as the experiment airfoil. The nondimensionalized geometry is shown on the right in Figure 1. The wing spans the entire vertical dimension of the test section (1.8 m) and has a chord of 150 mm. A total of 42 pressure orifices (21 on either side of the wing, as shown on the right in Figure 1) were used to measure the static pressure over the airfoil surface. The orifices were connected to pressure transducers with a sampling frequency of 331.6 Hz, and data were acquired for approximately 10s for each test cases.

PIV measurements were conducted using the apparatus shown in the schematic plot in Figure 2. The flow inside the tunnel was seeded with water-glycol droplets of 1 μ m of median diameter produced by a SAFEX smoke generator. The flow was illuminated by a Quantel Evergreen Nd:YAG laser (200 mJ of pulse energy, 15 Hz of repetition rate, 532 nm of wavelength). It created a 2-mm thin laser sheet. The measurement plane was located close to the midspan of the airfoil, avoiding the location of the pressure orifices used for pressure measurement. Flow field imaging in the wake of the airfoil was conducted using two LaVision's Imager sCMOS cameras (2560×2160 pixel, 16 bit, 6.5×6.5μ m-pixel size) with 50 mm of Nikon lenses using $f_{\#}$ of 4. This camera can capture two images with 120 ns of interframe time. Two cameras were mounted side by side so that a large field of view could be achieved, capturing the airfoil wake and the evolution of the vortex shedding. The averaged imaging magnification was $M = 0.05$ with a digital resolution of 8 pixels/mm. The cameras were controlled by a LaVision programmable timing unit PTU X, where precise pulses are triggered and synchronized for cameras and lasers. This PTU X is controlled through software DaVis 8.4 from LaVision GmbH. In the experiment, the acquisition frequency was set at 15Hz. For most test cases, 200 images were acquired for each camera; For the cases of AoA = 0°, 100 images were acquired. The convergence study can be found in Section C.

Pressure measurements were carried out for a wide range of AoA values: from 0° to 130° and from 175° to 310°. Note that the missing range from 130° to 175° and from 310° to 360 was due to the pitch limitation of the turning table of the setup. However, since our primary focus is on the high AoA, we chose to concentrate on the remaining angles that could be measured more readily. The test cases are shown in Table 2. It is important to note that we were unable to reach higher Reynolds numbers (*Re*) due to the relatively short (15 cm) chord length of the model

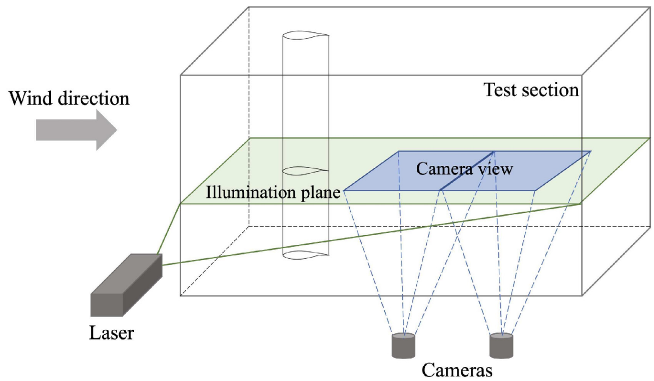

FIGURE 2 | PIV setup.

TABLE 2 | Test cases for the pressure measurement.

Re	Free-stream velocity U (m/s)	AoA
2×10^5	21.8	(For all *Re*) from 0° to 130° with 2° interval, 175°,
5×10^5	53.5	From 178° to 210° with 2° interval,
8×10^5	92.5	And from 215° to 310° with 5° interval

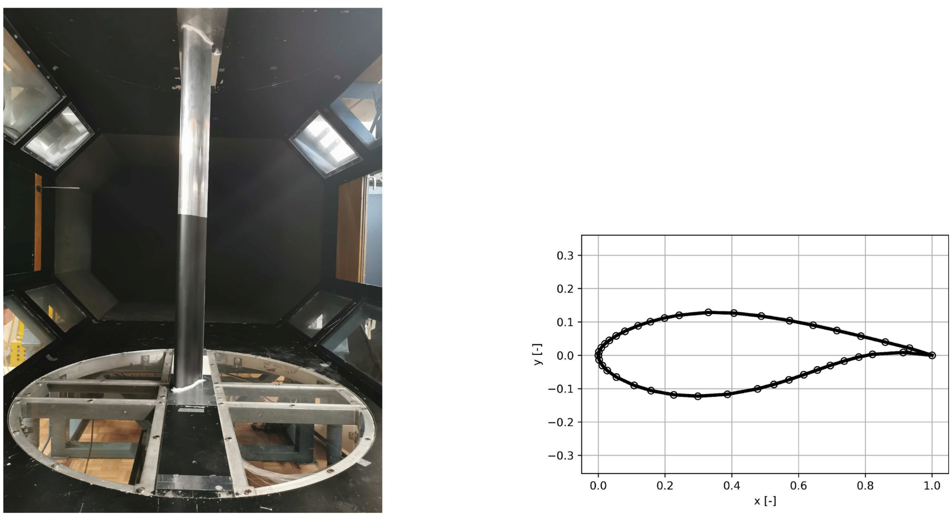

FIGURE 1 | Side view of the test section with the mounted airfoil (left) and the nondimensionalized geometry of airfoil DU91-W2-150 with locations of pressure taps marked with circles (right).

employed in this study. At large AoA and Re above 8×10^5, we observed significant tunnel and model vibrations accompanied by intense aeroacoustic noise. The maximum wind speed tested in this campaign is aligned with the maximum wind speed tested for high AoA values in this wind tunnel previously [21].

PIV measurements were carried out along with the pressure measurement. However, due to optical blockage in the cameras' fields of view, PIV measurements could be conducted only at AoA = 90°, 130°, 270°, and 310°.

2.2 | Data Processing Method

2.2.1 | Correction for Pressure Measurement System Dynamic Response

While measuring the unsteady pressure using the pressure measurement system, a certain delay and damping for the measurements can be expected due to geometrical features of the pressure measurement tubes and sensors. One way of correction is to use a transfer function to correct the data in the frequency domain. Using the MATLAB code *PreMeSys2GUI.m* based on the theory from [22], the transfer functions were calculated based on the pressure tube lengths, pressure tube radius, the volume of the cavity of the tubes, and so on. The corrected data in the frequency domain were then transformed in the time domain for further analysis. The transfer functions are shown in Section A.

2.2.2 | Wind Tunnel Wall Correction

Due to the presence of wind tunnel walls, the flow condition might be different around the airfoil compared to the condition where the airfoil is in the free air. Therefore, corrections should be applied to the raw pressure data before further analysis. Considering the condition that the flow is attached to the airfoil (at low AoA values) or separated from the airfoil (at large AoA values), there are two dominant correction methods, respectively, namely, Julian's method [23] and Maskell's method [24]. In this research, both methods are employed and compared. Details about these correction methods are reported in Section B.

2.2.3 | Aerodynamic Forces

The airfoil's lift and drag coefficient C_l and C_d are calculated as follows:

$$C_l = C_n \cos(\mathrm{AoA}) - C_t \sin(\mathrm{AoA}) \tag{1}$$

$$C_d = C_n \sin(\mathrm{AoA}) + C_t \cos(\mathrm{AoA}) \tag{2}$$

where C_n and C_t are the normal and tangential force coefficients and are calculated as follows:

$$C_n = \int_0^1 (C_{p_l} - C_{p_u}) d\frac{x}{c} \tag{3}$$

$$C_t = \int_0^1 (C_{p_u}\frac{dy_u}{dx} - C_{p_l}\frac{dy_l}{dx}) d\frac{x}{c} \tag{4}$$

where C_{p_u} and C_{p_l} are the pressure coefficient on the upper and lower surfaces of the airfoil and y_u and y_l are the y coordinates of the lower and upper surfaces.

2.2.4 | PIV and POD Analysis

The PIV recordings were processed with the Davis 8.4 software from LaVision GmbH. At each pixel location, the average intensity over a short sequence of 5 images was subtracted to eliminate the background light reflections. Due to the optical blockage of the lower structure of the wind tunnel test section, masks were defined for each test case where the blocked part was masked out of the flow field calculation. Then, the image recordings were processed with an iterative cross-correlation based algorithm with window deformation. The initial interrogation window size was set to 128×128 pixels with 50% overlap, while the final window size was set to 24×24 pixels with 75% overlap.

At large AoA values, due to the intrinsic characteristic of separated flow, POD analysis is conducted to identify the most energetic flow structures and flow dynamics in the airfoil's wake. POD is used to obtain low-dimensional descriptions of high-dimensional processes and is often used to extract modes from experimental data [25]. For example, a POD analysis was conducted to extract the most energetic physics from the wake of a blade in a compressor cascade [26]. Furthermore, the unsteady behavior of flow over an axisymmetric backward-facing step was examined using high-speed PIV and through POD of the PIV data [27]. Here, it was found that 50% of the total fluctuating energy is contained within the first 10 modes. The unsteady flow field around a square two-dimensional cylinder at incidence using PIV was studied [28]. POD analysis is confirmed to be an efficient method to describe the large-scale coherent wake motion when using the first two POD modes for the reconstruction of flow.

3 | Results and Discussion

3.1 | Time-Averaged Behavior

3.1.1 | Airfoil Aerodynamic Performance

The lift and drag polar of the DU91-W2-150 airfoil is shown in Figure 3 by taking the average of the unsteady data from the experiment. The performance for $Re = 5 \times 10^5$ and 8×10^5 is similar while that for 2×10^5 deviates: It has higher drag at 90° but lower drag and lift after 210°. This can mean that at $Re = 2 \times 10^5$ and at those AoA values, viscosity plays a larger role which has a greater influence on the airfoil than at other higher Re values.

As the airfoil passes through a wide range of AoA values, reverse flow can happen at specific locations as the geometric trailing edge is in the front which creates immediate separation. The illustration of the AoA values with respect to the wind is shown in Figure 4. Figure 5 shows the comparison between forward flow and reverse flow at three Re values. For the forward flow region of AoA between 0° and 90°, the

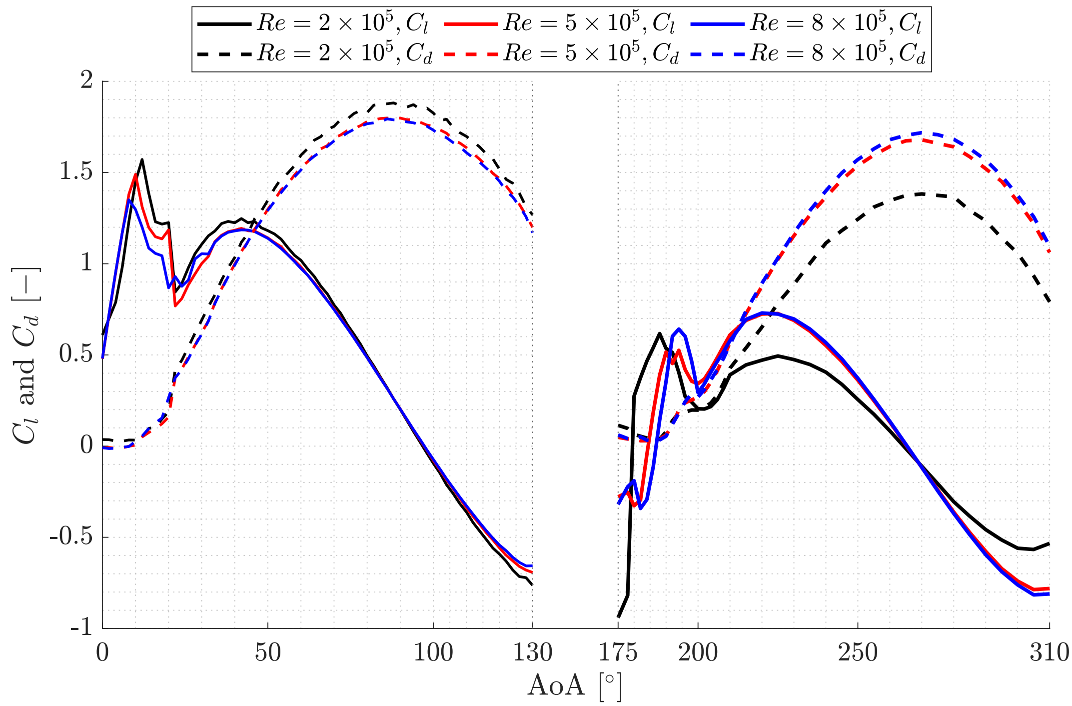

FIGURE 3 | Aerodynamic performance of DU91-W2-150 at three *Re* values.

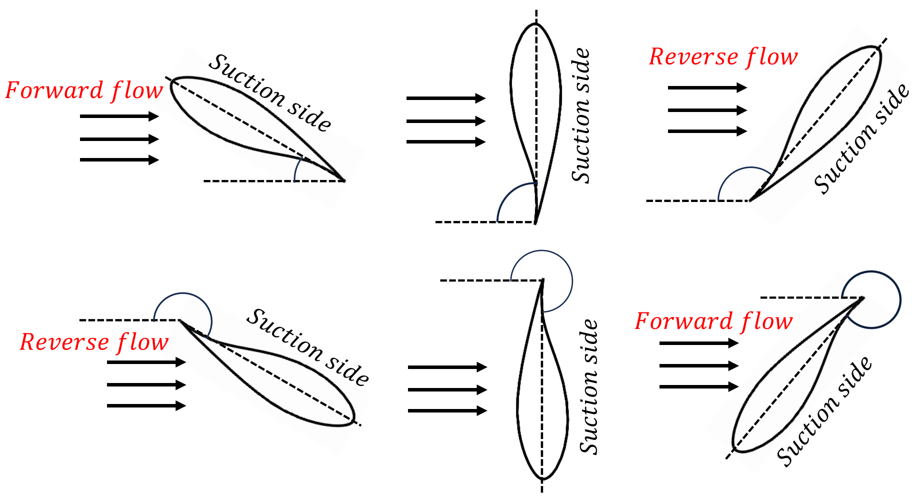

FIGURE 4 | Schemetic plot of different AoA values tested in the campaign. The wind comes from left to right. The corresponding AoA is 30°, 90°, and 130° for the first row and 210°, 270°, and 310° for the second row. When the geometric trailing edge is facing the front wind, reverse flow occurs.

comparison is made with the reverse flow region of AoA_{rev} from 180° to 270°. And AoA_{rev} is subtracted by 180° to match the comparison plot. Similarly, for the forward flow region of 270° to 310° (airfoil nose down), a fair comparison is made with AoA_{rev} from 90° to 130°. And AoA_{rev} here is added by 180° in the plot.

For AoA and AoA_{rev} −180° between 0° and 90°, the airfoil has higher C_l in forward flow conditions. In this condition, C_d is slightly higher despite slightly lower reverse flow conditions when AoA and $\mathrm{AoA}_{rev} - 180°$ is lower than 20°. However, when AoA and $\mathrm{AoA}_{rev} + 180°$ is between 270° and 310°, in general, the airfoil in the reverse flow condition has higher C_l and C_d.

As C_l and C_d are calculated from the pressure difference from the upper and lower surface, the C_p comparison between forward flow and the corresponding reverse flow condition is shown in Figure 6. For AoA = 40°, the local stagnation near the leading edge on the pressure side makes the pressure difference smaller than that for the corresponding AoA_{rev} case, which proves the higher lift in the forward flow case. When AoA = 270°, the pressure difference in the trailing edge region is smaller than that of the corresponding value at AoA_{rev} due to a different influence of separation on the pressure side, which gives a higher lift for the reverse flow condition. The above results show that no matter whether the flow is forward or reverse, as long as the concave surface is facing upwind as the pressure side, aerodynamic loads are in general higher. When

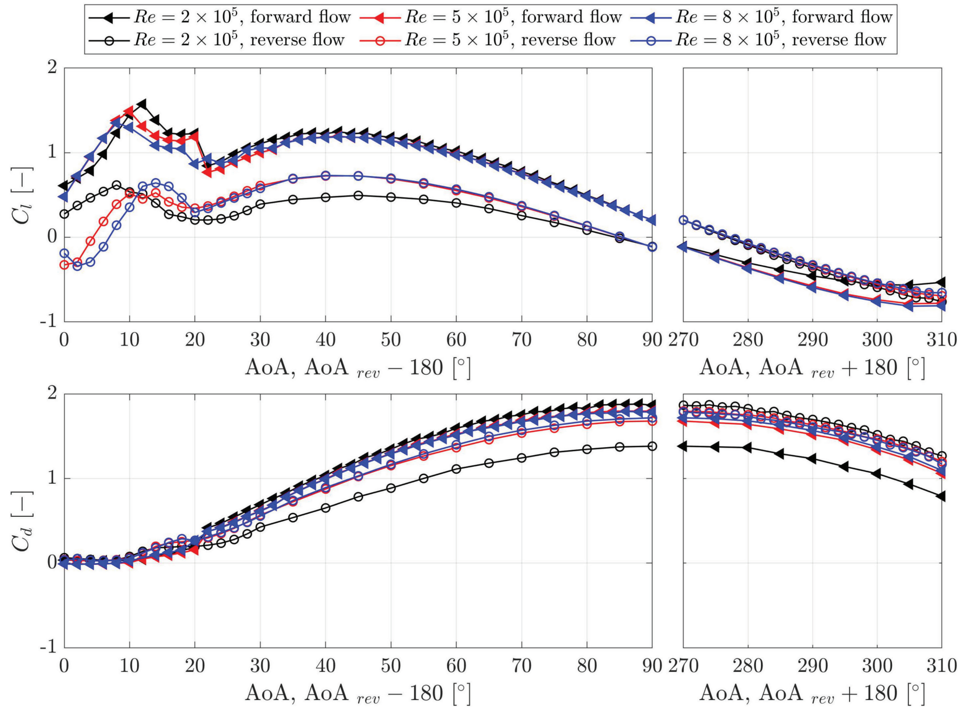

FIGURE 5 | Aerodynamic performance in forward flow and reverse flow conditions at three *Re* values.

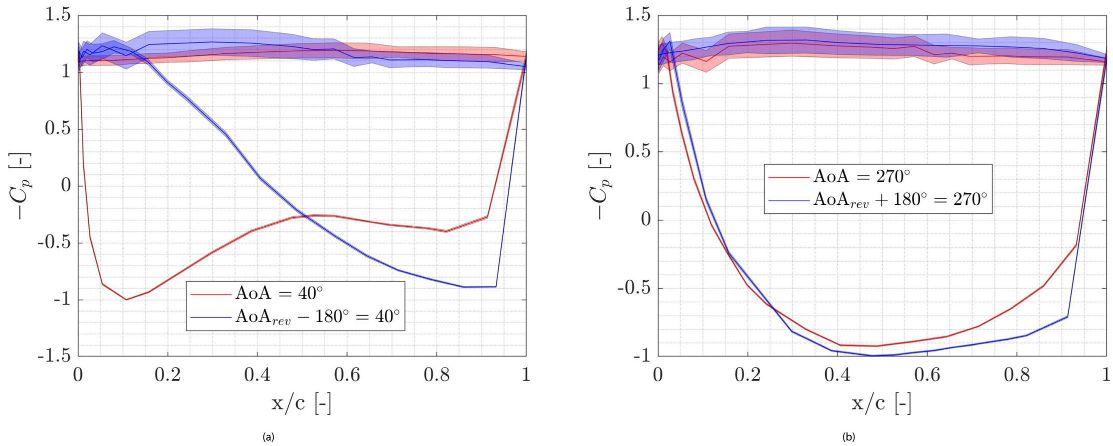

FIGURE 6 | Surface pressure comparison between forward flow and the corresponding reverse flow angle at $Re = 5 \times 10^5$. Shaded area represents the standard deviation.

AoA is between 0° and 90° and when $\mathrm{AoA}_{rev} + 180°$ is between 270° and 310° (AoA between 90° and 270°), the concave pressure side brings higher aerodynamic force as there might be local separation near the trailing edge concave area.

Figure 7 depicts C_l slope for the forward flow and reversed flow cases. When C_l slope is smaller than 0, the region is unfavorable for wind turbine blade structures as it indicates a higher possibility of negative aerodynamic damping, which can lead to structural instability [29]. This figure shows that the influence of *Re* is minimal, especially at large incidence angles (AoA ($\mathrm{AoA}_{rev} - 180$) larger than 25° and AoA ($\mathrm{AoA}_{rev} + 180$) between 270° and 310°). At these angle regions, $\partial C_l/\partial \alpha$ maintains slightly below zero, contributing marginally to negative aerodynamic damping. Before the static stall angle (approximately 10°), $\partial C_l/\partial \alpha$ presents an overall positive value for both forward flow and reverse flow cases. In contrast, after the static stall angle, $\partial C_l/\partial \alpha$ sharply drops to negative values with a minimum of approximately −0.18 from all the test cases. This sharp decline highlights a strong destabilizing effect, indicating a risk of structural instability near stall.

3.1.2 | Reynolds Effect on the Separation Point

The time-averaged surface pressures are plotted for all the measured *Re* values near the positive stall region in Figure 8. At AoA = 8°, the transition point to the turbulence region, indicated by the sudden drop of C_p, gets closer and closer to the leading edge as *Re* increases. At AoA = 10°, the flow is

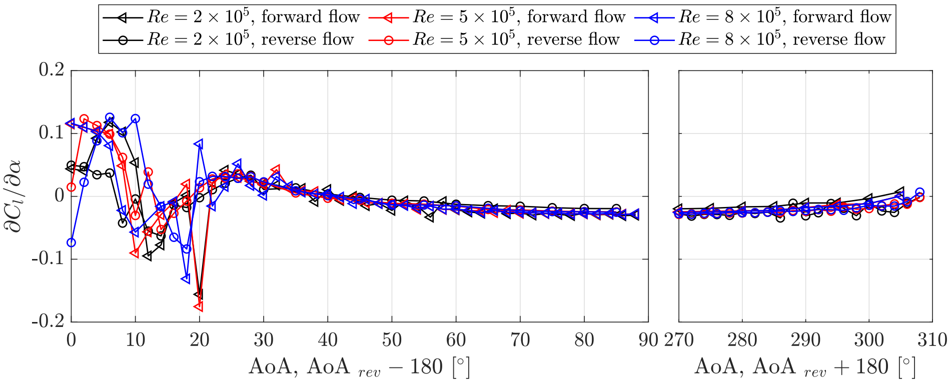

FIGURE 7 | C_l slope in forward flow and reverse flow conditions at three *Re* values.

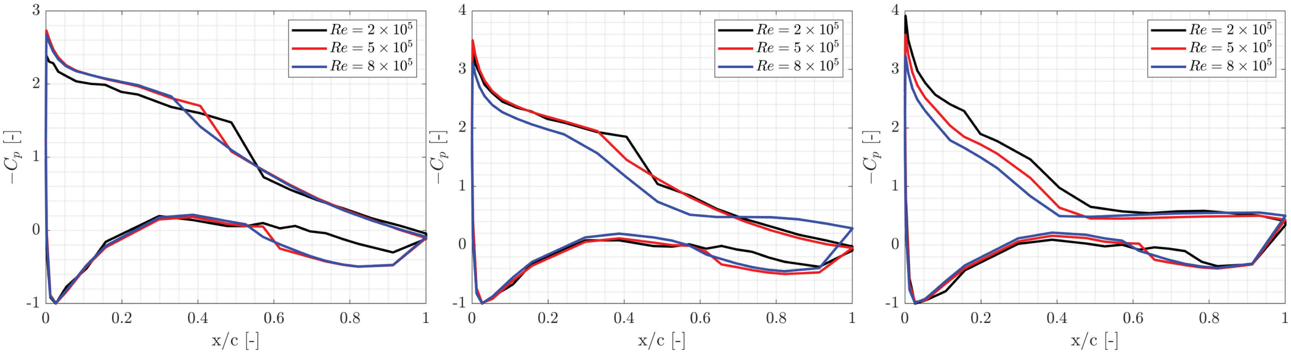

(a) AoA = 8° (b) AoA = 10° (c) AoA = 14°

FIGURE 8 | Pressure coefficient C_p near the possible stall region for all the measured *Re* values.

separated for $Re = 8 \times 10^5$, with a plateau after $x/c = 0.6$. For lower *Re* values, the flow remains attached despite of transition to a turbulent boundary layer. At AoA = 14°, flow is separated for all *Re* values, while the highest *Re* has the separation point more towards the leading edge. The experiment results align with the previous findings [4], indicating that a higher *Re* leads to an earlier stall. This is attributed to the increased dominance of viscous forces at lower *Re* values, promoting flow attachment to the surface.

Similarly, the surface pressures near the negative stall region from 188° to 198° are plotted for all the measured *Re* values in Figure 9. The *x*-axis is flipped in order to show the aerodynamic leading edge (the geometric trailing edge) first. The suction side is the concave surface which is the pressure side for the positive stall case. Different from the positive stall region, a local separation near the leading edge is happening, which can be seen for AoA up until 196° at $Re = 8 \times 10^5$, up until 194° at $Re = 5 \times 10^5$, up until 192° at $Re = 2 \times 10^5$. This is attributed to the sharp geometry of the leading edge, while it still follows the same separation order as the positive stall onset where lower *Re* induces earlier separation.

The separation locations for all *Re* values on the suction side of the airfoil are depicted in Figure 10. It is important to note that the plotted points correspond to locations that are fully separated up to the trailing edge, excluding those that have been reattached to the surface. Across all *Re* values, there is a distinct trend of the separation location moving towards the leading edge as the AoA increases. As AoA increases, at *Re* $= 2 \times 10^5$, the separation is the latest. For $Re = 8 \times 10^5$, separation happened the earliest as AoA increases to 20°. Then the separation remains in the same position at $x/c = 0.08$ for 6° more and slowly reaches the leading edge at AoA = 38°. As can be seen in Figure 3, the force at AoA region between 20° and 38° after the stall angle is highly nonlinear. Under high *Re* conditions, this situation worsens. The presence of small leading-edge vortices can quickly shed with rapid reattachment, causing the separation point not to remain fixed at the leading edge for this *Re*. This is illustrated by the suction peaks near the leading edge area in Figure 11.

3.1.3 | Surface Pressure

The time-averaged surface pressure at $Re = 5 \times 10^5$ is further compared for different AoA values and is shown in Figure 12. The two plots in the first row show the C_p surface for the AoA values measured on the suction side, while the two plots in the second row show the pressure side. Suction peaks are shown in the forward flow (AoA between 0° and 30°) and reverse flow (AoA between 180° and 270°) cases near the leading edge and trailing edge region, respectively. Due to the early separation at the aerodynamic leading edge, the suction peak region is smaller in reverse flow than that in a forward flow. The stagnation point on the pressure side ($-Cp = -1$) moves towards

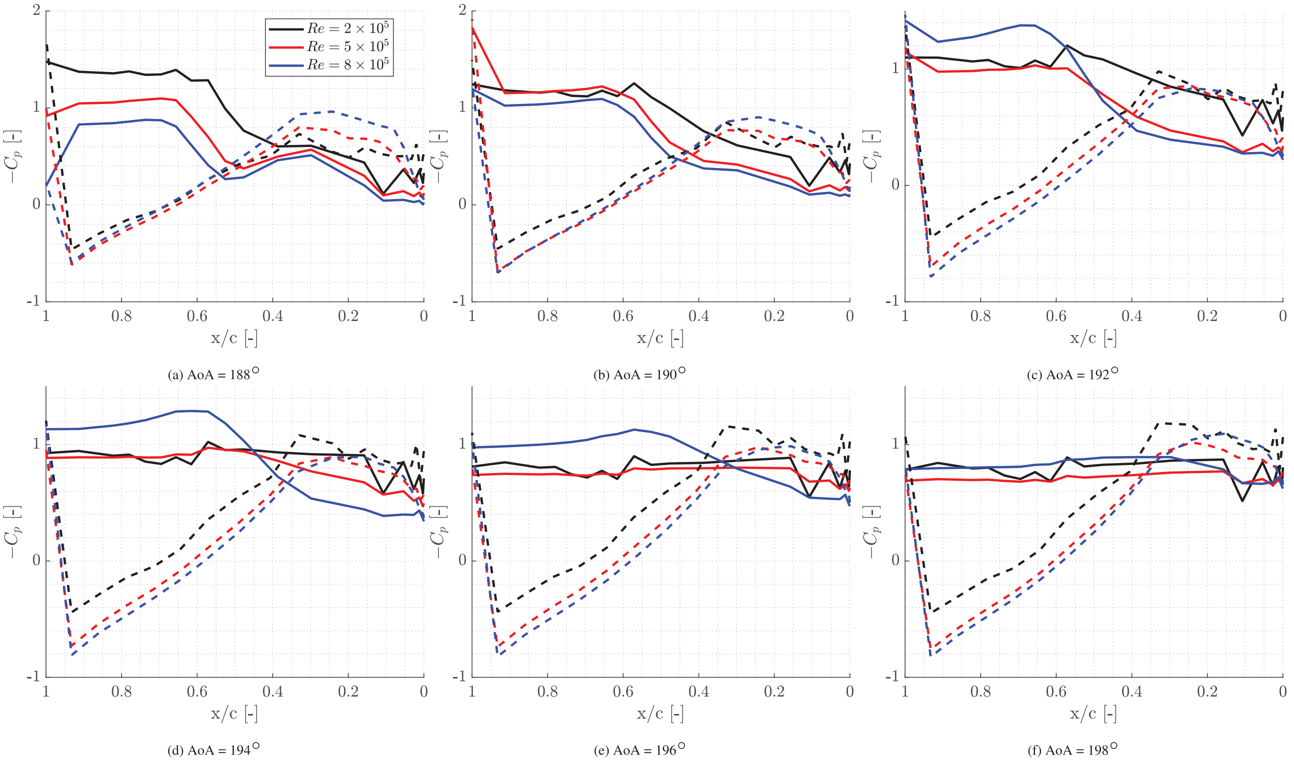

FIGURE 9 | Pressure coefficient C_p near the negative stall region for all the measured *Re* values. The *x* direction was flipped in the plot which shows the geometric leading edge first as it serves as the aerodynamic leading edge. The pressure side are shown as dashed in order for clarification.

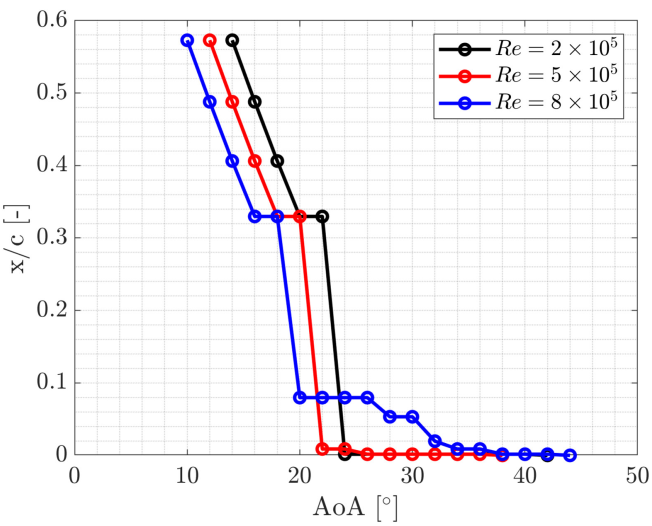

FIGURE 10 | Separation locations on the airfoil surface on the suction side for different *Re* values.

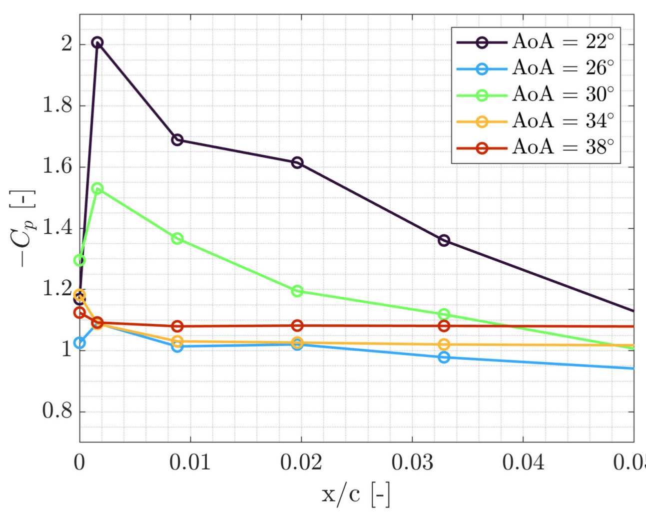

FIGURE 11 | Leading edge surface pressure for AoA from 20° to 38° at $Re = 8 \times 10^5$.

the trailing edge as AoA increases from 0° to 130° and moves back towards the leading edge as AoA goes from 180° to 310°. On the suction side, beyond AoA of 40° and 215°, the C_p surface smoothens and maintains a uniform distribution. The obtained results align with previous measurements [11] for the available results of AoA lower than 180°. As shown in Figure 3, the flow well exceeds the positive stall and negative stall onset region after these two AoA values (36° and 215°), which indicates that the flow does not undergo a sudden change in pressure; as in most instances, the flow is fully separated.

3.1.4 | PIV Mean Flow Field

Figure 13 shows the mean flow field and vorticity field at AoA = 90°, 270°, 130°, and 310° at $Re = 5 \times 10^5$. As shown in

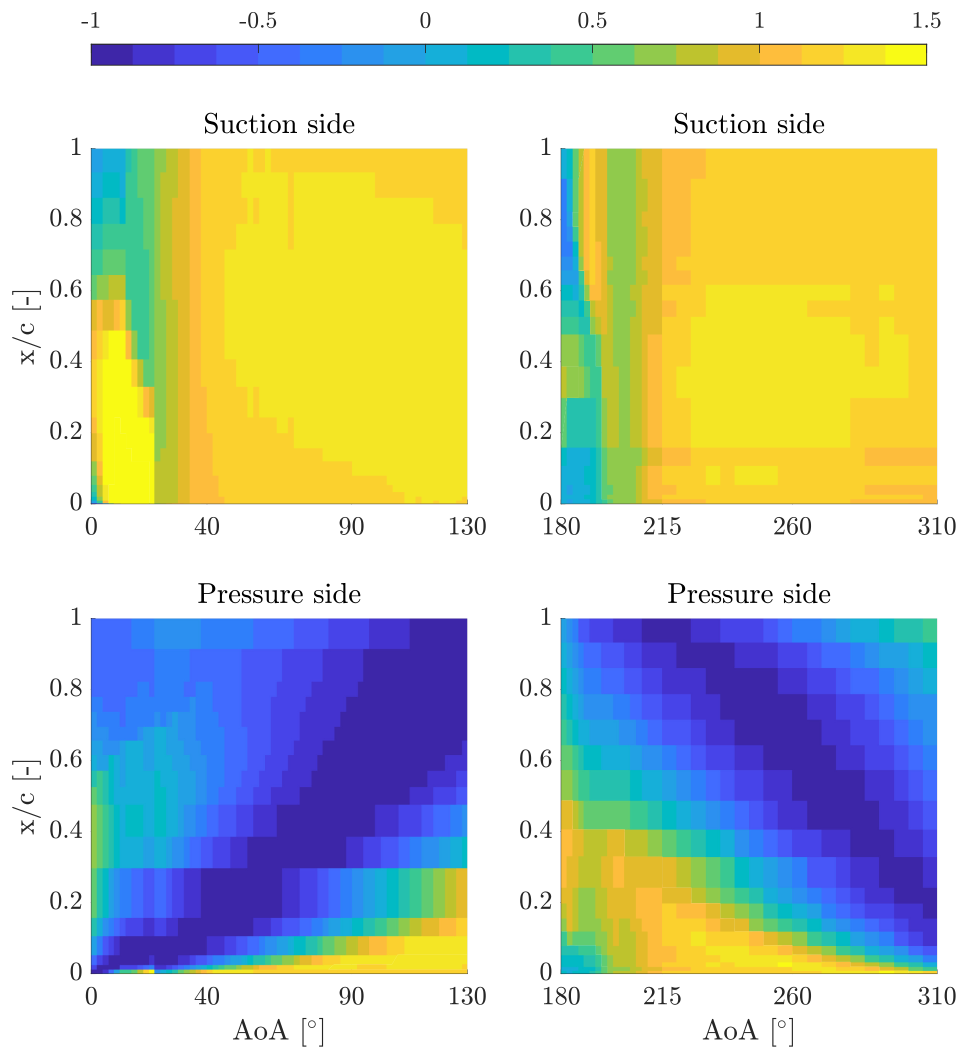

FIGURE 12 | Average of pressure coefficient $-C_p$ for all AoA values tested at $Re = 5 \times 10^5$. Note that the suction side is the different side for AoA larger than 180°.

Figure 13a, a region with stalled flow is shown near the middle of the chord at AoA = 90°. As a comparison, the result of AoA = 270° at $Re = 5 \times 10^5$ is presented here in Figure 13c,d. When AoA = 270°, the pressure side of AoA = 90° becomes the suction side. Due to the concave curvature of the aerodynamic suction side, the center of the wake (blue area in Figure 13c) shifts slightly towards the trailing edge.

This is also revealed in Figure 14a where the wake contour lines of $V_x/U = -0.2$, 0, 0.4 and 0.75 are plotted together with 90° cases. The 270° case has a faster wake recovery since it reaches the same speed with a shorter downwind distance compared with 90°. This reveals that convex and concave surfaces of the asymmetric airfoil create different aerodynamic effects on the airfoil. When AoA is below 180°, the concave surface is facing the wind. This surface will cause a drastic change to the flow field, which has a potential to expand the wake. On the other hand, when AoA is above 180°, the convex surface is facing upwind. This more streamlined surface has less influence on the flow field than the concave surface, which results in a faster recovery. This is also confirmed with the wake width comparison shown in Table 3 where the wake width of 90° at velocity $V_x/U = 0.75$ is wider than that of 270°.

Figure 13e–h presents the wake results for AoA = 130° and 310° at $Re = 5 \times 10^5$. Note that 310° is the angle where the leading edge and trailing edge swap their positions compared with 130°. For these two AoA values, the average flow fields (Figure 13e,g) and vorticity fields (Figure 13f,h) are similar, except for the locations of the maximum reverse velocity. This difference is also shown in Figure 14b, where the wake contour lines of $V_x/U = -0.2$, 0, 0.4 and 0.9 are plotted for 130° and 310°. This contour plot also shows a faster recovery and a smaller wake for 310° due to the upwind concave curvature where the reverse flow occurs. Compared with 90° and 270°, the wakes at 130 and 310° are narrower. At 130° and 310°, the projected length at the wind tunnel cross section is smaller, which leads to a smaller interference on the flow. When the airfoil is at 90° or 270°, the flow separates abruptly from the airfoil, giving a longer recovery time. While for 130° and 310°, the shorter projected length in the wind tunnel direction gives less blockage to the flow.

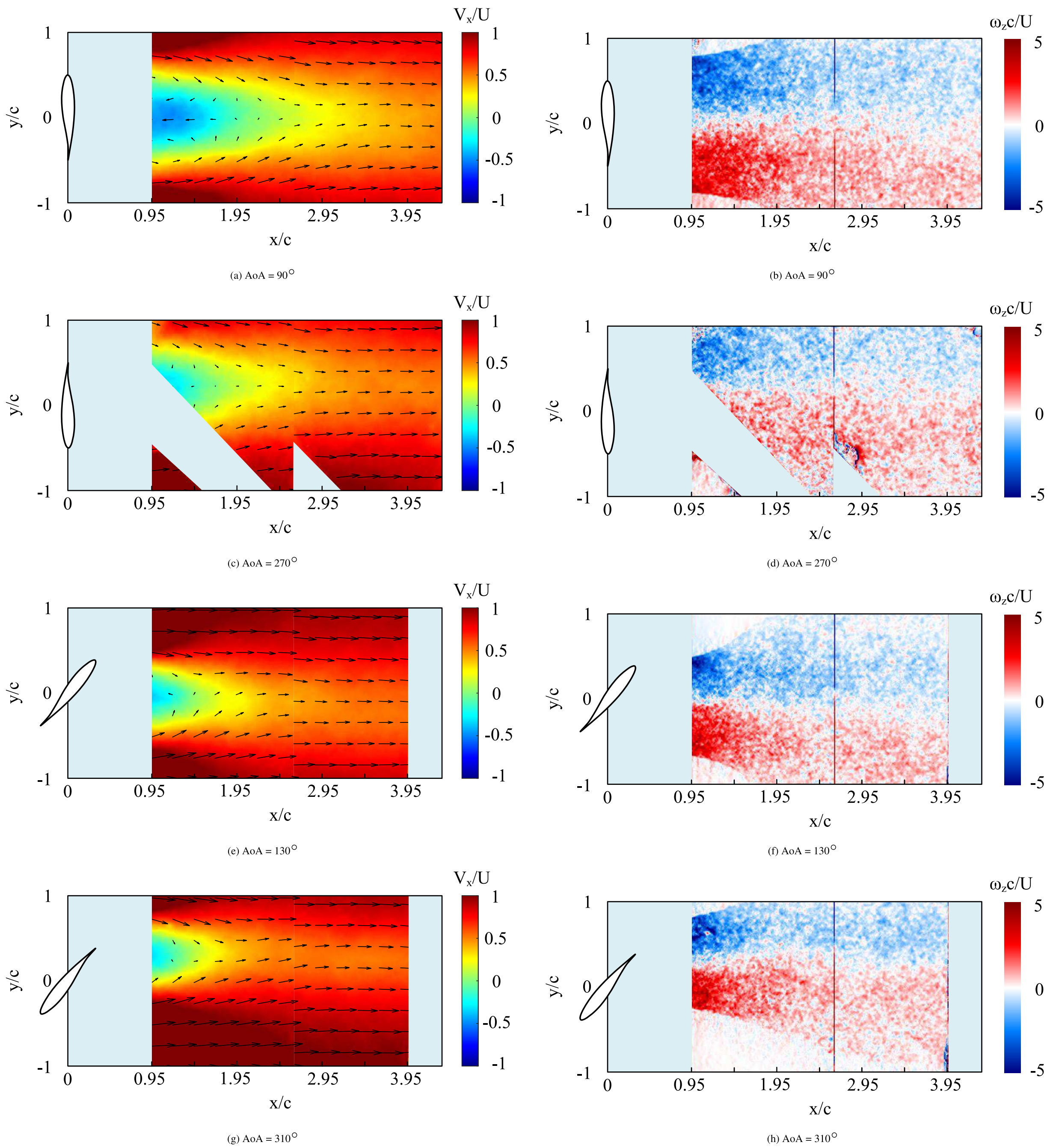

FIGURE 13 | Mean flow field (left column) and vorticity field (right column) at AoA = 90°, 270°, 130°, and 310°, $Re = 5 \times 10^5$.

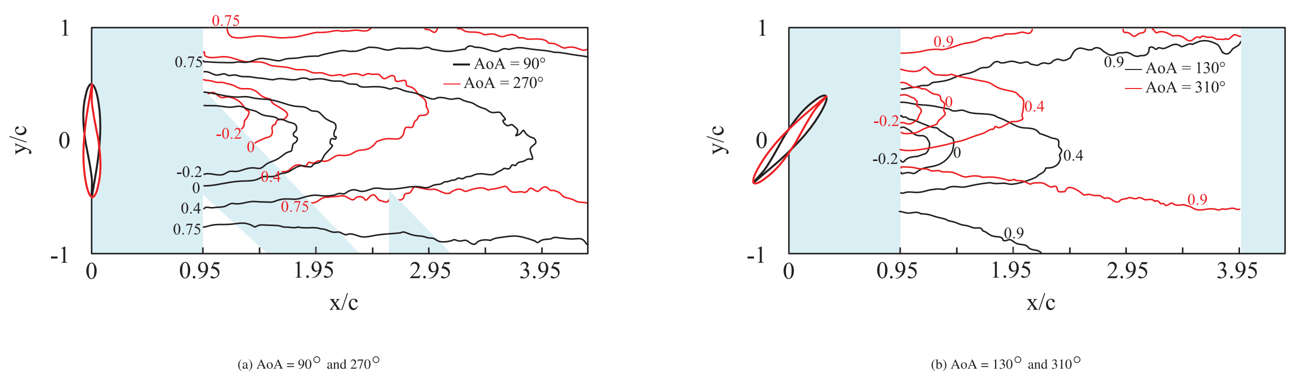

FIGURE 14 | Wake contour lines of $V_x/U = -0.2, 0, 0.4$ and $0.75(0.9)$ for several AoA values at $Re = 5 \times 10^5$. Note that the contour line $V_x/U = 0.75$ was plotted for 90° and 270° while $V_x/U = 0.9$ was plotted for 130° and 310°.

3.2 | Unsteady Behaviors

3.2.1 | Variations of C_l and C_d

Variations of time series of forces are examined to study the unsteadiness. Specifically, the influence of forward flow and reverse flow are compared and shown in Figure 15. Here, two times the standard deviation (2σ) is used to represent the overall fluctuation. When AoA or $\text{AoA}_{rev} - 180°$ is between 0° and 30°, the fluctuation of Cl remains relatively low (below 0.1), despite some spikes in the stall onset between 10° and 20° and between the corresponding negative stall region of $\text{AoA}_{rev} - 180$ between 10° and 20°. When AoA is between 20° and 30°, a higher 2σ is expected as the flow fluctuates near the leading edge region with an unfixed separation point, which is shown in Figure 10.

As the angle exceeds 30°, 2σ starts to increase for both C_l and C_d and $2\sigma(C_l)$ reaches the local maximum near 40° (220°). Afterwards, the flow remains fully separated and $2\sigma(C_d)$ stays at almost the same level while $2\sigma(C_l)$ slowly drops to below 0.05° to 90° (and 270°) as C_l slowly diminishes to near 0 as shown in Figure 3. In the nose-down region of 270° to 310° and its corresponding reverse flow region, an axis-symmetric variation pattern is shown compared to the range from 50° to 90°. In this region, $2\sigma(C_l)$ is the lowest for 270° (90° for AoA_{rev}) and gradually increases as AoA increases. Meanwhile, in general, the forward flow (indicated as triangle markers) has less fluctuation compared to reverse flow regions (indicated as the circle marker) in each *Re*. The higher fluctuation for the reverse flow cases is attributed to the earlier separation in the aerodynamic leading edge, which induced instability.

TABLE 3 | Wake width at four AoA values.

AoA (°)	Wake width D/c (-)	Location x/c (-)	Wake velocity V_x/U (-)
90	1.52	2	0.75
270	1.49	2	0.75
130	1.09	1	0.9
310	1.01	1	0.9

3.2.2 | POD Analysis

POD analysis results are presented in Figure 16 for AoA = 90°. The first two dominant modes in the streamwise direction from POD analysis are shown in Figure 16a,c for AoA = 90°. From the energy plot in Figure 17, the first mode accounts for 29.9% of the energy and the second accounts for 23.8%. Therefore, the first two modes take up more than half of the total energy, which makes the first two modes dominant in the flow movement. It can be seen from the structure that the first two modes are in the same shape and are paired. The dashed lines in the center of the peaks reveal the shift of one-quarter wavelength, which corresponds to a phase shift of 90°, which is in agreement with previous finding [30]. These two modes lead to the vortices shedding from the leading and trailing edges in turn and together formulate the sinusoidal shape wake, as shown from the wake reconstruction in Figure 16b. The temporal coefficients of the first two modes are plotted against each other in Figure 16d and the red circle represents the theoretical values. The scatter of the points in the vicinity are also an indication of the cyclic vortex-shedding process where the first two modes are paired.

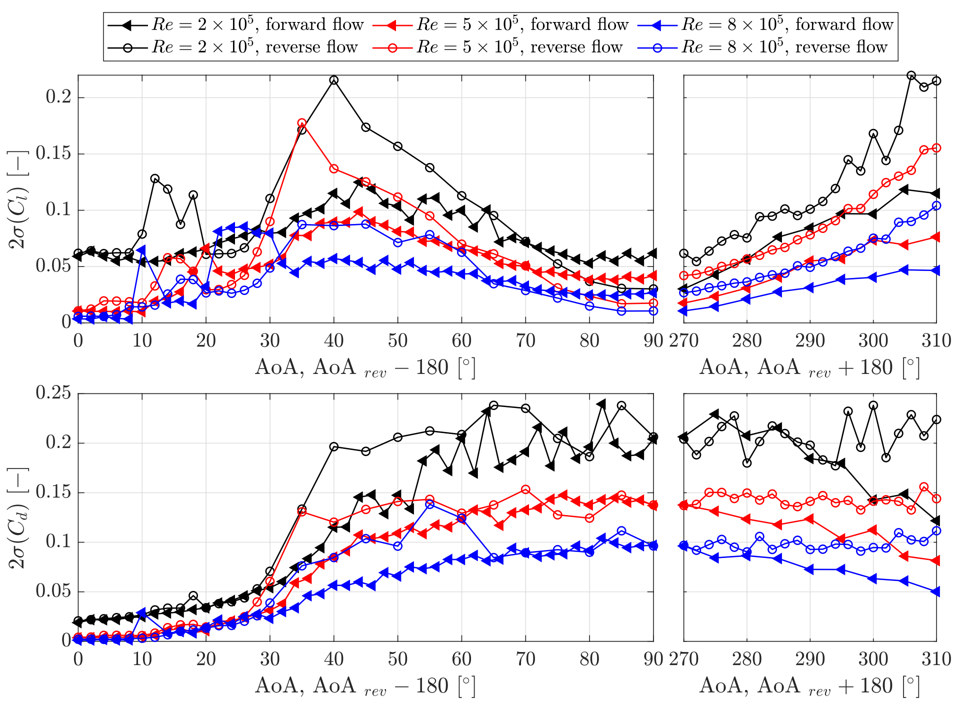

FIGURE 15 | Fluctuations (two times the standard deviation 2σ) of unsteady C_l and C_d for different *Re* values in the forward flow and reverse flow conditions.

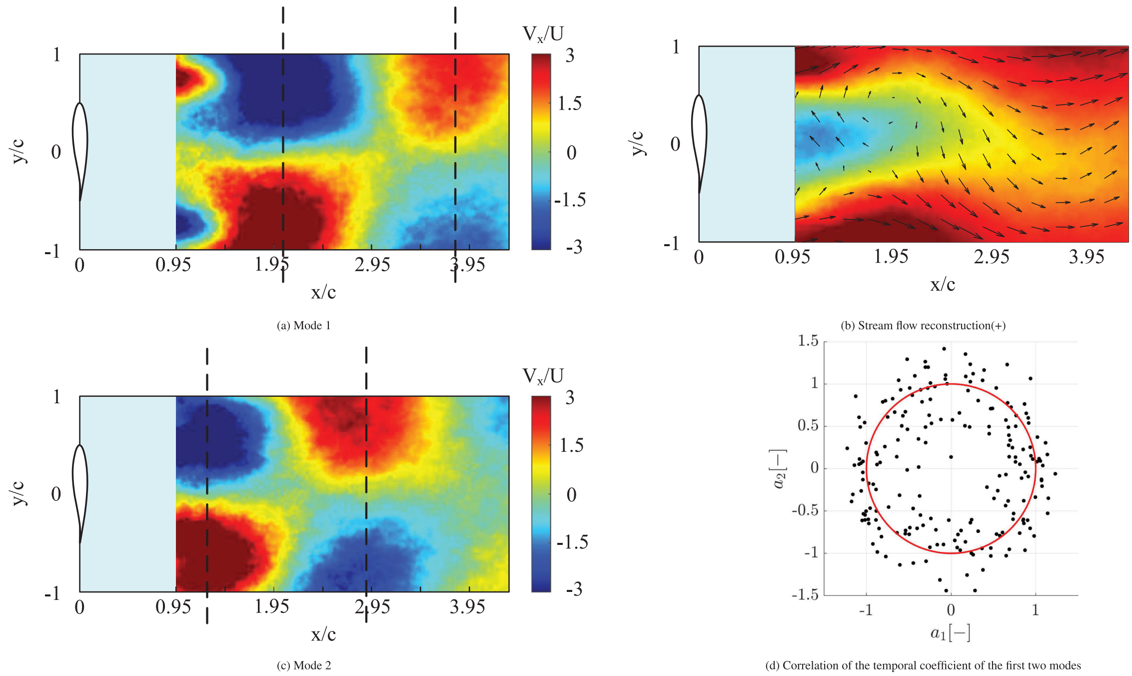

FIGURE 16 | POD mode analysis at AoA = 90°, $Re = 5 \times 10^5$. (a, c) First two modes. (b) Corresponding wake reconstruction based on the first two modes. (d) Correlation of the temporal coefficient of the first two modes.

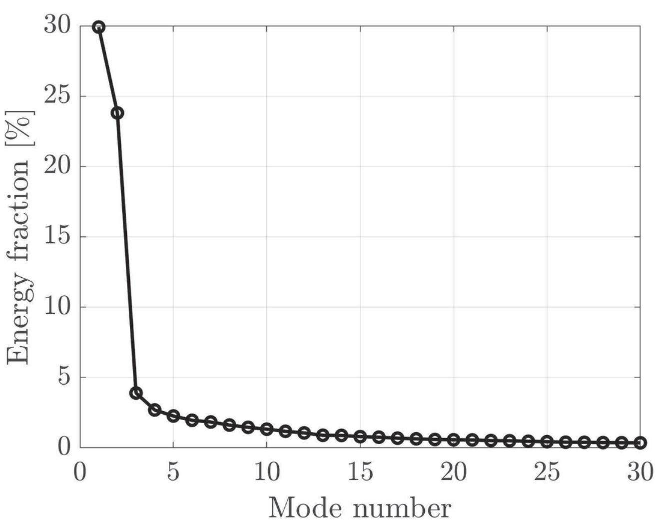

FIGURE 17 | Energy fraction for the first 30 modes at 90° in Re 5×10^5.

3.2.3 | Variation of Vortex Shedding Frequency and Corresponding St Number

The time series of corrected pressure was transformed into the frequency domain using the Welch method, where a flattop window was applied. By taking the Fast Fourier transform (FFT), the power spectrum density (PSD) of C_p at the suction surface under different AoA values at chordwise locations near the leading edge ($x/c = 0.05$), in the middle of the chord ($x/c = 0.49$) and in the trailing edge ($x/c = 1$) were plotted and shown in Figure 18 for $Re = 5 \times 10^5$. Owing to the periodicity of vortex shedding, the dominant peak shown in the FFT plot indicates the dominant vortex shedding frequency. For Figure 18a (10°) and Figure 18b (190°), the FFT for each chordwise location is mixed together and they do not show a dominant peak. As these two AoA values are in the vicinity of stall, the aerodynamic force experiences large variations and nonperiodic vortex shedding which makes the process unstable. Thus, multiple shedding frequencies can occur and the dominant shedding frequency is not obvious in the FFT plot.

The vortex shedding frequencies are different if one considers forward flow and reverse flow. Differences can be found in the last three rows of subfigures in Figure 18. For AoA at 30°, 50°, and 90°, the shedding frequency is always slightly smaller than the corresponding cases in AoA at 210°, 230°, and 270°. This also coincides with the result of the wake contours in Figure 14 which shows a thinner wake when the convex surface is facing upwind and undergoing reverse flow. A thinner wake results in a higher shedding frequency due to a smaller projected length in the flow. It is also noted that all the subfigures show a wide range of high-power spectral density at low frequencies. This may be due to the vibration of the model.

The dominant peak for each AoA is plotted with regard to AoA in Figure 19a. It is noted that when AoA = 90° (Figure 18g), the dominant peak occurs near 56 Hz, and a second peak near 112 Hz is observed, which is likely the first harmonic (twice the frequency) of the fundamental 56 Hz peak. The vortex shedding frequency is nondimensionalized into St as shown in Figure 19b where St is calculated as $St = fc\,\sin(\mathrm{AoA})/U$. Here, the characteristic length used for calculating St is the projection length of the chord (c) in the cross-section plane of the wind tunnel. It is noted that in order to obtain the dominant frequency more precisely, FFT of C_l was used for finding the peaks. This is because C_l takes the integral of the surface pressure; therefore, the small

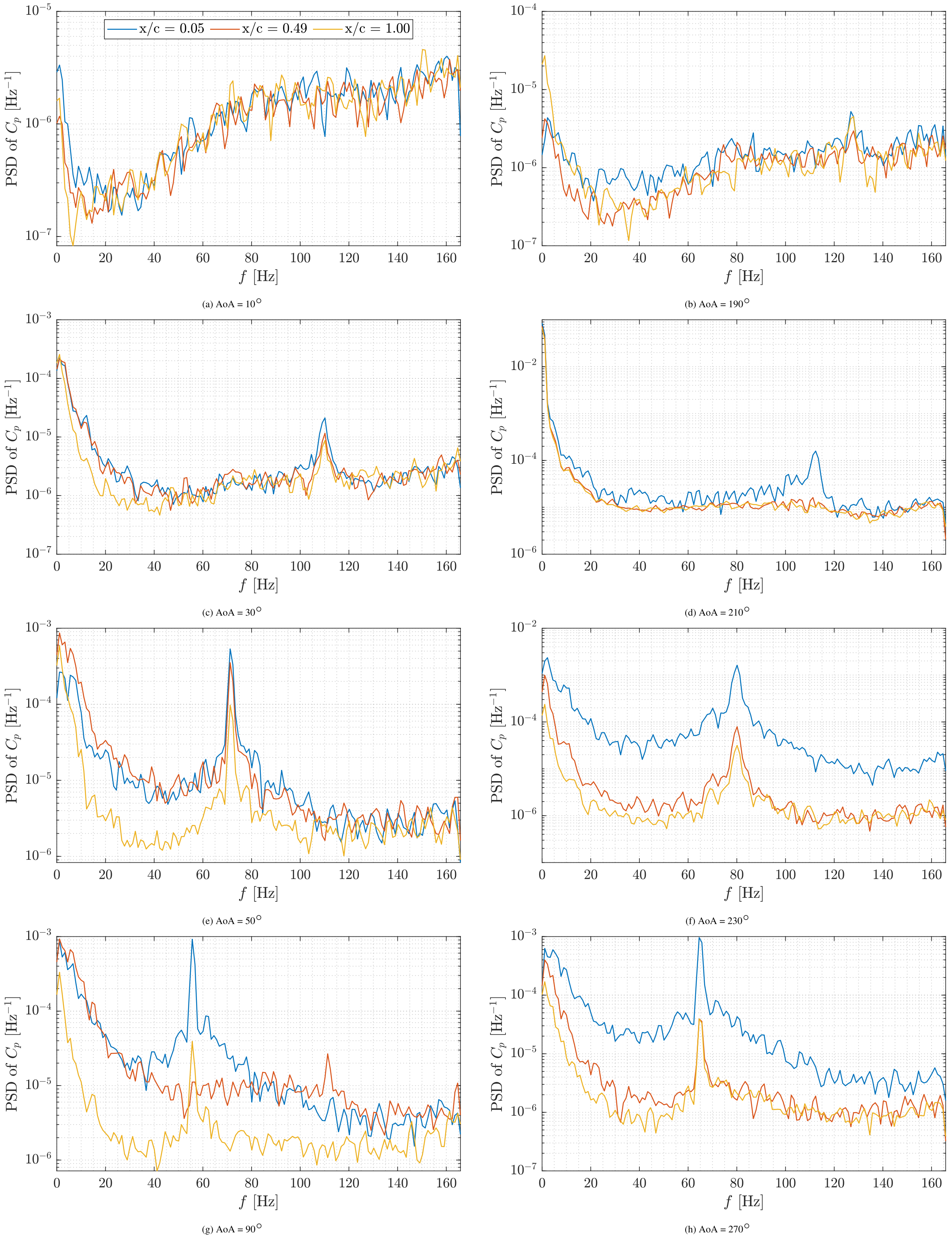

FIGURE 18 | FFT of C_p at airfoil suction surface at $Re = 5 \times 10^5$.

peaks shown in the FFT of C_p will be minimized and the dominant peak will be more noticeable.

Figure 19a shows that for AoA between 0° and 180° and between 180° and 360°, the vortex shedding frequency follows the same trend: it drops until 90° (or 270°) and then increases after that. A similar trend can be seen for frequencies of different *Re* values, with higher shedding frequency at the higher Reynolds number. Although the vortex shedding frequency is sensitive to *Re*, the corresponding *St* is not influenced by the tested three *Re* values or AoA. In Figure 19b, *St* at different *Re* values collapse onto one single curve, remaining almost constant for different AoA values although with minor fluctuations. This uniformity is due to the full stall characteristics of the airfoil, where the

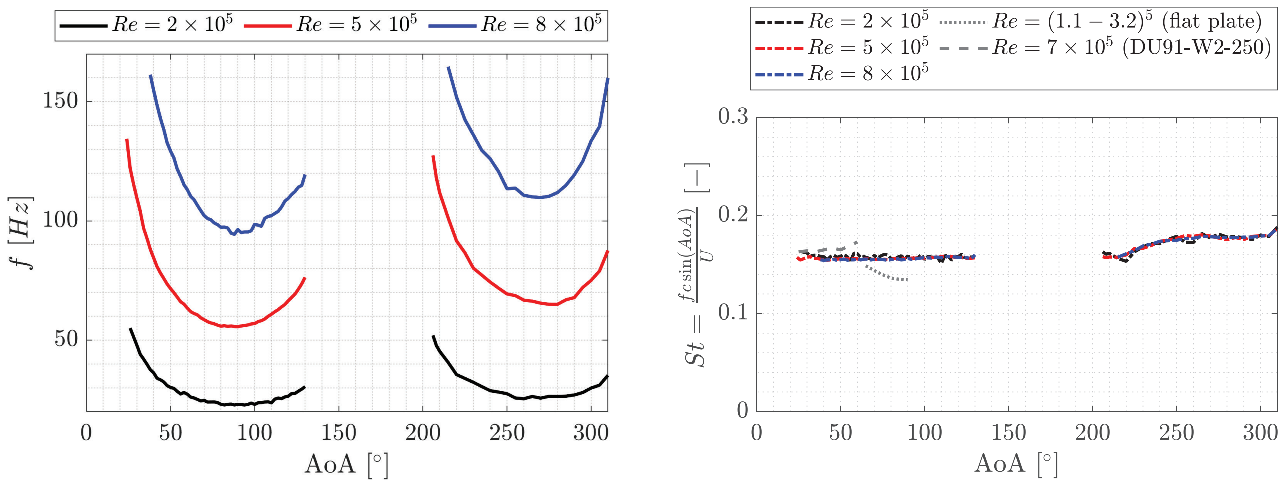

(a) Vortex shedding frequency

(b) Strouhal number calculated with projected height

FIGURE 19 | Vortex shedding frequency and Strouhal number calculated with projected height. The result of St at $Re = (1.1 - 3.2) \times 10^4$ for a flat plate [31] and the result for DU91-W2-150 at 7×10^5 [20].

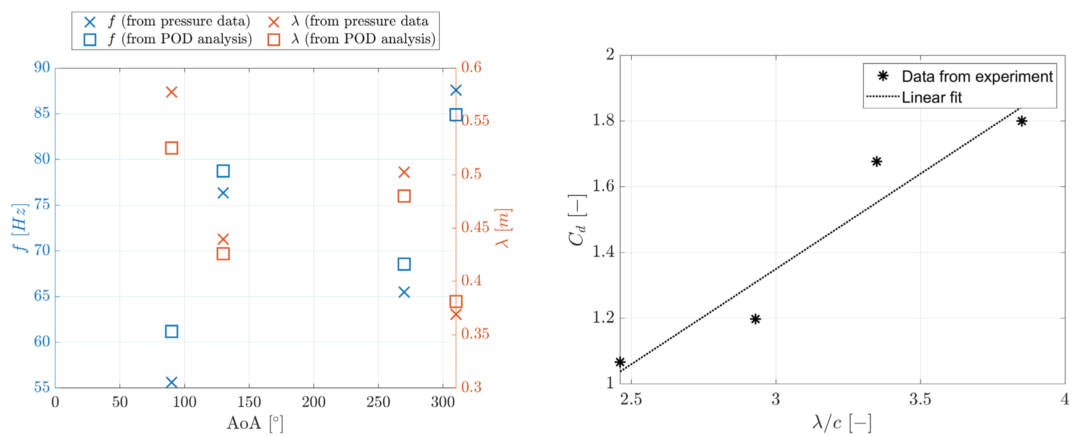

(a) Comparison of frequency and wave length (λ)

(b) The relation of drag coefficient with wave length (λ)

FIGURE 20 | Comparison of frequency and wavelength (λ) from experiment measurement and from POD analysis (left) and the relation of drag coefficient with wavelength (λ). On the right figure, the data from experiments from left to right are the case of AoA 310°, 130°, 270°, and 90°.

flow is dominated by flow separation. In this condition, the vortices are mainly shed from the edges of the airfoil and the shedding process is not influenced by neither Re nor AoA. Previous research [31] showed a similar result. In their research, the universal St of the shedding frequency has been found at large AoA values from 65° to 90° for a flat plate with beveled sharp edges. The result is also replotted in Figure 19b. The St of the flat plate has a slightly lower value than that of the airfoil, which may be due to a difference in the Re (in the order of 10^3 and 10^4 in their campaign) and model geometry. In addition, an experiment was conducted in the same laboratory with the same airfoil but with different thicknesses [20]. A possible explanation for the higher St from that campaign can be a larger influence of the blockage effect, which influences slightly the vortex shedding frequency, flow speed, and so on.

It is noted that St at AoA lower than 130° matches the flat plate St of 0.16 [32]. When AoA is larger than 180°, St increases to between 0.16 and 0.18. This is mainly due to the convex upwind curvature of the airfoil, which leads to higher vortex shedding frequencies and St. This finding significantly proves the consistency of St while also providing a more detailed comparison when there is a reverse flow for an asymmetric airfoil.

Apart from obtaining vortex shedding frequency from the pressure measurement, the shedding frequency can also be extracted from the modes shown in POD. In Figure 16c for AoA 90°, half of the wavelength (the length from the two neighboring peaks in the streamwise direction) is approximately $1.76c$. With the wake velocity obtained from PIV, the shedding frequency is $63Hz$, which matches that obtained from the pressure data in Figure 19a. The vortex shedding frequency and corresponding wavelengths for the cases at $Re = 0.5 \times 10^5$ are concluded in Figure 20a for AoA =90°, 270°, 130°, and 310°. The difference between POD analysis and the pressure measurement mainly comes from the limited spatial resolution to determine the distance (λ) and the averaged wake velocity in PIV data (approximately 60% free stream velocity) when calculating the estimated frequency.

The wake of the flow is strongly influenced by the force experienced by the airfoil. As depicted in Figure 20, the impact of drag on vortex shedding in the wake conforms to a linear relationship. This can be attributed to two factors. Firstly, this is related to the blockage of the airfoil to the flow. When an airfoil has a relatively large angle, it projects a longer length in the wind, which leads to a larger C_d. This explains the trend from the group of AoA = 90° and 270° and the group of 130° and 310°. On the other hand, in the case of 90° and 270° (or the case of 130° and 310°), although the relative angle is the same in each case, due to the upwind convex characteristic of the airfoil surface for AoA 270° and 310°, these two AoA values have slightly lower drag. And since the upwind convex surface has a smaller impact to expand the wake, these two AoA values also have shorter vortex wavelengths. Hence, these two reasons account for the linear relationship as shown.

4 | Conclusion

In this paper, an experimental research is presented to study the unsteady aerodynamic performance of a DU91-W2-150 airfoil under a wide range of AoA values up until 310° at three *Re* values at the magnitude of 10^5 using pressure measurement and PIV technique. The experimental data for large AoA values are valuable either for future fundamental airfoil study or wind turbine study at stand still condition. A wide variety of effects were studied. Four conclusions can be drawn from the analysis here.

- *Effect of airfoil geometry on the mean airfoil load*: The plot of C_l and C_d for the forward flow and reverse flow shows that no matter the direction of the flow, as long as the concave surface is facing upwind, the aerodynamic loads are higher. The wake contour lines of AoA = 90°, 270°, 130°, and 310° further validate this result.
- *Effect of Re on the separation on the airfoil*: The separation point on the airfoil was found based on the previous theory and for all three *Re* values tested in the campaign, the separation points tend to move towards the leading edge as AoA increases. For this DU91-W2-150 airfoil, as *Re* increases from 2×10^5 to 8×10^5, separation tends to happen earlier for both the positive stall and the negative stall. This is mainly due to that the viscous force is less dominant in the flow as *Re* increases. For the highest *Re* tested, local separation very close to the leading edge happened just before the positive stall onset as the high *Re* flow induces instabilities in the flow.
- *Effect of forward flow and reverse flow*: The 2σ plot of C_l and C_d indicates that reverse flow induces more fluctuations compared to forward flow. This is attributed to the occurrence of separation at the aerodynamic leading edge in a reverse flow scenario, as shown in the surface pressure plot as well.
- *Vortex shedding frequency and Strouhal number*: The vortex shedding frequency matches with the frequency estimated from POD, where the vortex shedding wavelengths show a strong relation with airfoil drag. The result from normalized *St* reveals that *St* remains approximately constant at large AoA values despite different *Re* and AoA values, due to full stall characteristics. Meanwhile, *St* is slightly higher when AoA is larger than 180° as an airfoil with a convex curvature in the upwind direction has a smaller effect to expand the wake, thus higher shedding frequency.

Conflicts of Interest

The authors declare no conflicts of interest.

Data Availability Statement

The data that support the findings of this study are openly available in 4TU. Research Data with DOI:10.4121/c42b2fe5-5df6-4518-ab26-604502f311cc.

Peer Review

The peer review history for this article is available at https://www.webofscience.com/api/gateway/wos/peer-review/10.1002/we.2974.

References

1. J. G. Leishman, "Challenges in Modelling the Unsteady Aerodynamics of Wind Turbines," *Wind Energy: An International Journal for Progress and Applications in Wind Power Conversion Technology* 5, no. 2-3 (2002): 85–132.

2. H. Schlichting and K. Gersten, *Boundary-Layer Theory* (Berlin Heidelberg: Springer, 2016).

3. N. J. Kay, P. J. Richards, and R. N. Sharma, "Influence of Turbulence on Cambered and Symmetrical Airfoils at Low Reynolds Numbers," *AIAA Journal* 58, no. 5 (2020): 1913–1925.

4. F. Bertagnolio, H. A. Madsen, A. Fischer, and C. Bak, "A Semi-Empirical Airfoil Stall Noise Model Based on Surface Pressure Measurements," *Journal of Sound and Vibration* 387 (2017): 127–162.

5. L. W. Traub and E. Cooper, "Experimental Investigation of Pressure Measurement and Airfoil Characteristics at Low Reynolds Numbers," *Journal of Aircraft* 45, no. 4 (2008): 1322–1333.

6. K. Swalwell, J. Sheridan, and W. Melbourne, "Frequency Analysis of Surface Pressures on an airfoil after stall," in *21st AIAA Applied Aerodynamics Conference* (Orlando, FL, 2003), 3416.

7. S. Yarusevych and M. S. H. Boutilier, "Vortex Shedding of an Airfoil at Low Reynolds Numbers," *AIAA Journal* 49, no. 10 (2011): 2221–2227.

8. R. Gerakopulos and S. Yaruseyvich, "Novel Time-Resolved Pressure Measurements on an Airfoil at a Low Reynolds Number," *AIAA Journal* 50, no. 5 (2012): 1189–1200.

9. W. A. Timmer, "Aerodynamic Characteristics of Wind Turbine Blade Airfoils at High Angles-of-Attack," *TORQUE 2010: The science of Making Torque From Wind* 1 (2010): 71–78.

10. A. H. Lind and A. R. Jones, "Vortex Shedding From Airfoils in Reverse Flow," *AIAA Journal* 53, no. 9 (2015): 2621–2633.

11. A. H. Lind and A. R. Jones, "Unsteady Airloads on Static Airfoils Through High Angles of Attack and in Reverse Flow," *Journal of Fluids and Structures* 63 (2016): 259–279.

12. A. Pellegrino and C. Meskell, "Vortex Shedding From a Wind Turbine Blade Section at High Angles of Attack," *Journal of Wind Engineering and Industrial Aerodynamics* 121 (2013): 131–137.

13. P. W. Bearman, "Vortex Shedding From Oscillating Bluff Bodies," *Annual review of fluid mechanics* 16, no. 1 (1984): 195–222.

14. C. H. K. Williamson and R. Govardhan, "Vortex-Induced Vibrations," *Annual Review of Fluid Mechanics* 36 (2004): 413–455.

15. J. C. Heinz, N. N. Sørensen, F. Zahle, and W. Skrzypiński, "Vortex-Induced Vibrations on a Modern Wind Turbine Blade," *Wind Energy* 19, no. 11 (2016): 2041–2051.

16. W. Skrzypiński, M. Gaunaa, and J. Heinz, "Modelling of Vortex-Induced Loading on a Single-Blade Installation Setup," *Journal of Physics: Conference Series* 753 (2016): 82037.

17. A. Grille Guerra, C. Mertens, J. Little, and B. van Oudheusden, "Experimental Characterization of an Unsteady Laminar Separation Bubble on a Pitching Wing," *Experiments in Fluids* 64, no. 1 (2023): 16.

18. D. Ragni and C. Ferreira, "Effect of 3D Stall-Cells on the Pressure Distribution of a Laminar NACA64-418 Wing," *Experiments in Fluids* 57, no. 8 (2016): 127.

19. C. Simão Ferreira, G. Van Kuik, G. Van Bussel, and F. Scarano, "Visualization by PIV of Dynamic Stall on a Vertical Axis Wind Turbine," *Experiments in Fluids* 46 (2009): 97–108.

20. K. Boorsma, "Comparison of Experimental and Computational Aerodynamic Section Characteristics of Du91-W2-250 Profile" (Master's Thesis, 2003).

21. W. A. Timmer and R. P. J. O. M. Van Rooij, "Some Aspects of High Angle-of-Attack Flow on Airfoils for Wind Turbine Application," in *EWEC Copenhagen* (Denmark, 2001).

22. H. Bergh and H. Tijdeman, "Theoretical and Experimental Results for the Dynamic Response of Pressure Measuring Systems," Report NLR-TR F.238 (National Aero- and Astronautical Research Institute Amsterdam, 1965).

23. W. A. Timmer, "Wind Tunnel Wall Corrections for Two-Dimensional Testing up to Large Angles of Attack," in *Handbook of Wind Energy Aerodynamics*, eds. B. Stoevesandt, G. Schepers, P. Fuglsang, and S. Yuping (Cham: Springer, 2021), https://doi.org/10.1007/978-3-030-05455-7_27-1.

24. E. C. Maskell, "A Theory of the Blockage Effects on Bluff Bodies and Stalled Wings in a Closed Wind Tunnel," Aeronautical Research Council London (United Kingdom, 1963).

25. A. Chatterjee, "An Introduction to the Proper Orthogonal Decomposition," *Current Science* 78 (2000): 808–817.

26. L. Shi, H. Ma, and X. Yu, "Pod Analysis of the Unsteady Behavior of Blade Wake Under the Influence of Laminar Separation Vortex Shedding in a Compressor Cascade," *Aerospace Science and Technology* 105 (2020): 106056.

27. F. F. J. Schrijer, A. Sciacchitano, and F. Scarano, "Spatio-Temporal and Modal Analysis of Unsteady Fluctuations in a High-Subsonic Base Flow," *Physics of Fluids* 26, no. 8 (2014).

28. B. W. Oudheusden, F. Scarano, N. P. Hinsberg, and D. W. Watt, "Phase-Resolved Characterization of Vortex Shedding in the Near Wake of a Square-Section Cylinder at Incidence," *Experiments in Fluids* 39 (2005): 86–98.

29. K. Wang, V. A. Riziotis, and S. G. Voutsinas, "Aeroelastic Stability of Idling Wind Turbines," *Wind Energy Science* 2, no. 2 (2017): 415–437.

30. S. M. Hasheminasab, S. M. H. Karimian, S. Noori, M. Saeedi, and C. Morton, "Experimental Investigation of the Wake Dynamics for a NACA0012 Airfoil With a Cut-in Serrated Trailing-Edge," *Physics of Fluids* 33, no. 5 (2021): 55122.

31. J. M. Chen and Y.-C. Fang, "Strouhal Numbers of Inclined Flat Plates," *Journal of Wind Engineering and Industrial Aerodynamics* 61, no. 2-3 (1996): 99–112.

32. C. Tropea, A. L. Yarin, and J. F. Foss, *Springer Handbook of Experimental Fluid Mechanics*, Vol. 1 (Springer, 2007).

33. J. B. Barlow, W. H. Rae, and A. Pope, *Low-Speed Wind Tunnel Testing* (John wiley & sons, 1999).

34. Q. Ye, F. F. J. Schrijer, and F. Scarano, "Boundary Layer Transition Mechanisms Behind a Micro-Ramp," *Journal of Fluid Mechanics* 793 (2016): 132–161.

35. A. Sciacchitano and B. Wieneke, "PIV Uncertainty Propagation," *Measurement Science and Technology* 27, no. 8 (2016): 84006.

Appendix A

Dynamic Response of Pressure Measurement System

The transfer function for phase delay and amplitude ratio are calculated. The results are shown in Figure A1 for the concave and convex surface based on the tubes they are connected to the pressure transducer.

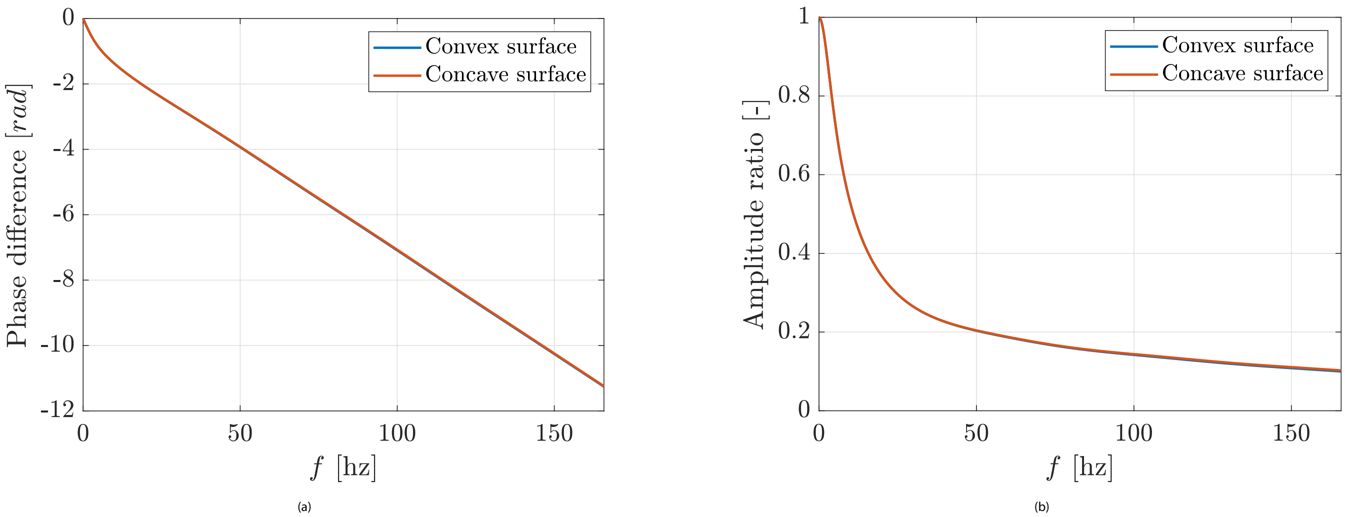

FIGURE A1 | Transfer function in the frequency domain for dynamic response correction of the pressure measurement system.

Appendix B

Wind Tunnel Wall Correction Method

Note that parameters with a prime refer to the uncorrected values.

B.1 | Julian's method [23]

In Julian's method, the pressures on the upper surface C_{p_u} and lower surface C_{p_l} are corrected as follows:

$$C_{p_u} = 1 - \frac{\left[\left(\frac{\sqrt{q_u^*}+\sqrt{q_l^*}}{2}\right)^2 + \left(\frac{q_u^*-q_l^*}{4} - \left(\frac{\sigma}{\pi\beta^2} - 5.25\frac{\sigma^2}{\pi\beta^4}\right)C_l'\sqrt{1-\left(1-\frac{2x}{c}\right)^2}\right)\right]^2}{\left(\frac{\sqrt{q_u^*}+\sqrt{q_l^*}}{2}\right)^2} \tag{B1}$$

$$C_{p_l} = 1 - \frac{\left[\left(\frac{\sqrt{q_u^*}+\sqrt{q_l^*}}{2}\right)^2 - \left(\frac{q_u^*-q_l^*}{4} - \left(\frac{\sigma}{\pi\beta^2} - 5.25\frac{\sigma^2}{\pi\beta^4}\right)C_l'\sqrt{1-\left(1-\frac{2x}{c}\right)^2}\right)\right]^2}{\left(\frac{\sqrt{q_u^*}+\sqrt{q_l^*}}{2}\right)^2} \tag{B2}$$

q_u^* and q_l^* are calculated as follows:

$$q_u^* = (1 - C_{p_u}')\frac{q'}{q} \tag{B3}$$

$$q_l^* = (1 - C_{p_l}')\frac{q'}{q} \tag{B4}$$

and the dynamic pressure ratio $\frac{q'}{q}$ can be obtained from the following:

$$q = q'\left[1 + \frac{2 - M'^2}{\beta^3}\Lambda\sigma\left(1 + \frac{1.1\beta}{(t/c)}\alpha^2\right) + \frac{(2 - M'^2)(1 + 0.4M'^2)}{4\beta^4}\left(\frac{c}{h}\right)C_d'\right] \tag{B5}$$

where M' is the uncorrected Mach number, $\frac{t}{c}$ is the relative thickness of the arfoil, and $\frac{c}{h}$ is the ratio of chord length and the width of the test section. The body-shape factor Λ, tunnel blockage factor σ, and the Prandtl–Glauert compressibility factor β are defined in Equation (B6), Equation (B7), and Equation (B8), separately:

$$\Lambda = \int_0^1 \frac{y}{c}\sqrt{(1 - C_p)\left(1 + \left(\frac{dy}{dx}\right)^2\right)}\, d\frac{x}{c} \tag{B6}$$

$$\sigma = \frac{\pi^2}{48}\left(\frac{c}{h}\right)^2 \tag{B7}$$

$$\beta = \sqrt{1 - M'^2} \tag{B8}$$

In addition, the corrected AoA α is calculated as follows:

$$\alpha = \alpha' + \frac{\sigma}{2\pi\beta}(C_l' + 4C_m') \tag{B9}$$

B.2 | Maskell's Method [24]

In Maskell's method, the pressure is corrected as follows:

$$C_p = 1 - \frac{1 - C_p'}{q/q'} \tag{B10}$$

Here the dynamic pressure ratio q/q' is calculated as follows:

$$\frac{q}{q'} = 1 + \epsilon\left(\frac{c}{h}\right)C_d \tag{B11}$$

The blockage factor for the bluff-body flow ϵ is recommended as 0.96 for 2D flow [24].

B.2.1 | Comparison Between Two Methods

The two correction methods for the wind tunnel blockage effect were compared for the case $Re = 8 \times 10^5$; the results are shown in Figure B1. When the angle between chord line and inflow is within 30° (AoA in the range of 0° to 30° and 175° to 210°), the two correction methods exhibit a small difference. However, when the angle is outside of this range, the two corrections start to diverge. The most notable difference is at approximately 90°

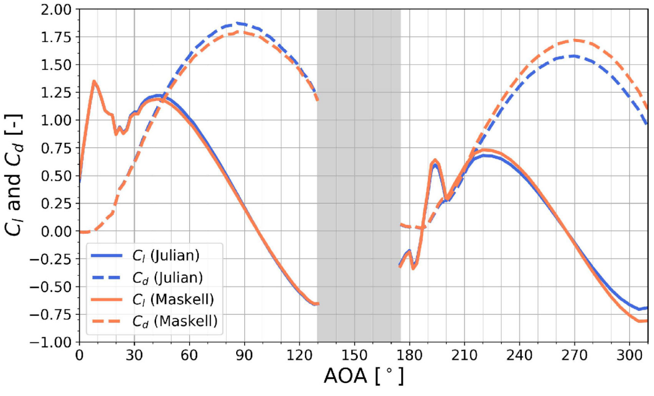

FIGURE B1 | Comparison of two blockage correction method for $Re = 8 \times 10^5$ (Gray area represents the AoA values that out of range of measurement).

and 270° for C_d and in the vicinity of the second peak for C_l. Because Maskell's method is known to provide more accurate corrections for separated flows [33], the latter is selected for further analysis.

Appendix C

Convergence Analysis of PIV Measurement

Since obtaining the mean flow field is the main goal of this PIV setup, it is of vital importance to check the convergence of the result to obtain good-quality data. At small AoA of 0°, 100 images were sampled, while at the other AoA values, 200 images were sampled. Figure C1 shows the evolution of mean flow velocity and Reynolds stresses with regard to the number of samples at $Re = 5 \times 10^5$. The maximum number of samples at AoA = 0° is 100, while that for AoA = 90° is 200. The mean flow velocity at 0° converges quickly, and the Reynolds stresses remain at a very low value close to 0. This means that 100 samples will keep a good quality of 0° cases. At AoA = 90°, the convergence happens after the averaging of 100 samples while a bit unstable for the Reynolds stresses R_{yy}, which the periodic vortex shedding disturbs heavily in the cross flow direction. Considering both accuracy and processing efficiency, 200 samples were deemed sufficient.

Appendix D

PIV Uncertainty

The standard uncertainty of the PIV measurements can be estimated from the ensemble data size and the flow velocity fluctuation [34]. For AoA = 0°, 100 uncorrelated snapshots were taken, while for the rest of the AoA values, 200 uncorrelated snapshots were taken; hence, the standard uncertainty of the phase-average flow velocity is equal to the following:

$$\varepsilon_u = \frac{\sigma_u}{U_\infty \sqrt{N}} \tag{D1}$$

σ_u is the representative standard deviation value of the streamwise velocity component (σ_u / U_∞ is approximately 0.1 in the wake of the wing) and N represents the number of uncorrelated samples. The standard uncertainty for the measurement cases is listed in Table D1.

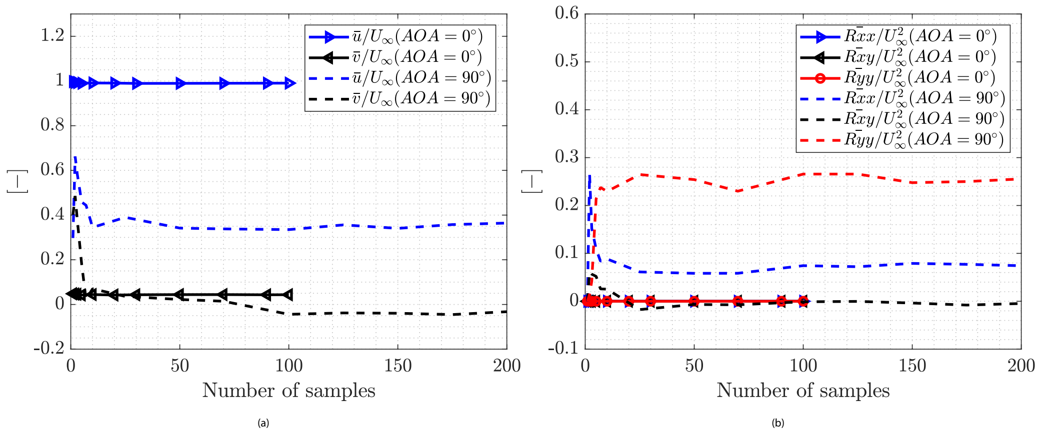

FIGURE C1 | Evolution of the statistical (a) average velocity and (b) Reynolds stresses at $Re = 5 \times 10^5$ at AoA = 0° and 90°.

TABLE D1 | Uncertainty of the PIV measurements.

	ε_u		$\varepsilon_{u'}$	
Re	**AoA = 0**	**AoA ≠ 0°**	**AoA = 0°**	**AoA ≠ 0°**
2×10^5	1%	0.7%	0.7%	0.5%
5×10^5	1%	0.7%	0.7%	0.5%
8×10^5	1%	0.7%	0.7%	0.5%

The uncertainty of the Root Mean Square (RMS) of the velocity fluctuations is estimated as follows [35]:

$$\varepsilon_{u'} = \frac{\sigma_u}{U_\infty \sqrt{2(N-1)}} \tag{D2}$$

And the uncertainty of the RMS of the velocity fluctuations for the measured cases is listed in Table D1.